Computational Geosciences (2018) 22:815–832
https://doi.org/10.1007/s10596-018-9727-7

ORIGINAL PAPER

A distributed parallel multiple-relaxation-time lattice Boltzmann method on general-purpose graphics processing units for the rapid and scalable computation of absolute permeability from high-resolution 3D micro-CT images

F. O. Alpak[1,2] · F. Gray[3] · N. Saxena[1] · J. Dietderich[1] · R. Hofmann[1] · S. Berg[4,5]

Received: 25 July 2017 / Accepted: 19 January 2018 / Published online: 19 March 2018

Abstract
Digital rock physics (DRP) is a rapidly evolving technology targeting fast turnaround times for repeatable core analysis and multi-physics simulation of rock properties. We develop and validate a rapid and scalable distributed-parallel single-phase pore-scale flow simulator for permeability estimation on real 3D pore-scale micro-CT images using a novel variant of the lattice Boltzmann method (LBM). The LBM code implementation is designed to take maximum advantage of distributed computing on multiple general-purpose graphics processing units (GPGPUs). We describe and extensively test the distributed parallel implementation of an innovative LBM algorithm for simulating flow in pore-scale media based on the multiple-relaxation-time (MRT) model that utilizes a precise treatment of body force. While the individual components of the resulting simulator can be separately found in various references, our novel contributions are (1) the integration of all of the mathematical and high-performance computing components together with a highly optimized code implementation and (2) the delivery of quantitative results with the simulator in terms of robustness, accuracy, and computational efficiency for a variety of flow geometries including various types of real rock images. We report on extensive validations of the simulator in terms of accuracy and provide near-ideal distributed parallel scalability results on large pore-scale image volumes that were largely computationally inaccessible prior to our implementation. We validate the accuracy of the MRT-LBM simulator on model geometries with analytical solutions. Permeability estimation results are then provided on large 3D binary microstructures including a sphere pack and rocks from various sandstone and carbonate formations. We quantify the scalability behavior of the distributed parallel implementation of MRT-LBM as a function of model type/size and the number of utilized GPGPUs for a panoply of permeability estimation problems.

Keywords Lattice Boltzmann method · LBM · Multiple-relaxation-time · MRT · Digital rock physics · DRP · Pore-scale flow simulation · Permeability · Upscaling · Computational fluid dynamics · CFD · General-purpose graphics processing unit · GPGPU · Parallel computing

✉ F. O. Alpak
Omer.Alpak@shell.com

[1] Shell International Exploration and Production Inc., 3333 Highway 6 S, Houston, TX 77082, USA

[2] Department of Computational & Applied Mathematics, Rice University, 6100 Main Street - MS 134, Houston, TX 77005, USA

[3] Qatar Carbonates and Carbon Storage Research Centre, Department of Chemical Engineering, Imperial College London, South Kensington Campus, London, SW7 2AZ, England

[4] Shell Global Solutions International B.V., Badhuisweg 3, 1031 CM Amsterdam, The Netherlands

[5] Department of Earth Science & Engineering, Department of Chemical Engineering, Imperial College London, South Kensington Campus, London, SW7 2AZ, England

1 Introduction

Digital rock physics (DRP) technology is a rapidly evolving multidisciplinary tool for computing rock properties (e.g., porosity, permeability, formation factors, resistivity index vs. water saturation (I-Sw) curves, capillary pressure curves, relative permeability) and characterizing microstructural attributes using high-resolution images (e.g., x-ray computerized tomography, scanning electron microscopy) [1–3, 5, 6, 9, 10, 12, 15, 22, 23, 37–39, 51, 58–60, 60–63]. The focus of the work documented in this paper is on the computation of absolute permeability by use of single-phase incompressible flow simulations performed on high-resolution three-dimensional (3D) image volumes of porous media by use of a robust and efficient implementation of the lattice Boltzmann method (LBM) [8, 34, 70, 71].

The LBM is a member of the lattice gas and lattice Boltzmann family of methods for simulating fluid flow. The mesoscale lattice Boltzmann model overcomes the noisy small-scale dynamics and lack of Galilean invariance problems of the lattice gas models [49]. As such, they have superseded lattice gas models for most applications. In the low Mach number limit, the Boltzmann equation reduces to the incompressible Navier-Stokes equation. The LBM solves a discrete continuum-scale form of the Boltzmann equation on a grid. The advantages of LBM over alternative methods are (1) relatively more straightforward handling of solid-fluid boundaries, (2) rapid convergence as a pressure solver, and (3) superior distributed-parallel scalability. Because of its computational efficiency and algorithmic simplicity, the LBM has become standard for computational fluid dynamics (CFD) based on simulation problems in a large number of fields. In this work, we describe and extensively test a novel LBM-based simulator for very fast distributed-parallel single-phase pore-scale flow simulations to compute velocity and pressure fields, and thereby, estimate the permeability of large binary (pore-and-rock) models in porous media.

The motivation for the development of a very fast and robust LBM algorithm for solving the absolute permeability estimation problem on large pore-scale images is summarized as follows: There are several commercial finite-volume/finite-element method (FVM/FEM)-based CFD codes available that simulate pore-scale flow [4, 20, 54]. However, they are too computationally demanding and not designed for running simulations directly on complex domains that are supplied by pore-scale imaging without an iterative (and generally cumbersome) mesh generation step. Moreover, they are too slow for realistic problem sizes and unfeasible for practical work. There are relatively fast commercial LBM and FVM codes available [18, 50, 73, 75]. Having stated that, not all of the commercial tools deliver a good compromise of accuracy against computational performance [61]. Moreover, access to the code for flexible customization and optimization is unavailable in this mode of operation. On the other hand, there are open source LBM codes available in the literature [45, 46, 52] but they are not computationally effective for realistic problem sizes. Moreover, they lack the robustness and rigor to serve as an industry-grade simulation tool. Thus, we develop, validate, and apply a very fast and robust LBM algorithm, which lends itself naturally to computation on multiple general-purpose graphics processing unit (GPGPU) nodes, using a massively parallel programming paradigm. The promise here is accessing the multi-core compute performance that stems from modern GPGPUs to solve direct numerical simulation problems of relevant size for DRP workflows.

We describe and test an algorithm for simulating flow in pore-scale media based on the multiple-relaxation-time (MRT) model accompanied by a precise treatment of the body-force term. The Boltzmann equation is discretized in space, velocity (momentum), and time coordinates using a 3D 19-velocity grid (D3Q19 scheme), which provides a good compromise between accuracy and computational efficiency since it utilizes a sufficiently large number of velocity components for accuracy, for example, larger than the D3Q15 scheme, but without being overly computationally demanding unlike, for instance, the D3Q27 scheme. The benefits of the MRT model over the conventional single-relaxation time Bhatnagar–Gross–Krook (BGK) model [13] are (I) enhanced numerical stability in the incompressible flow limit and at relatively high Reynolds numbers, (II) independent bulk and shear viscosities, and (III) viscosity-independent, non-slip boundary conditions. The drawback of the MRT model is that it is slightly more computationally demanding compared to the BGK model. We discuss the results of our efforts to accelerate pore-scale flow simulations via MRT-LBM algorithm on multiple GPGPUs. We implement all major computational elements of the MRT-LBM algorithm on GPGPUs via the Compute Unified Device Architecture (CUDA) programming language and utilizing domain-decomposition and asynchronous data exchange protocols for enhanced computational performance. It is important to highlight that the latter is a requirement rather than a choice, because this is the only way to access sufficient compute performance to reach acceptably low compute times for relevant problem sizes. The above combination of algorithms and hardware enables the simulation of pore-scale models with billions of voxels in minutes, thereby enabling fast permeability computations on real rock images. The individual components of the MRT-LBM-based simulator were described in various references. The novel contribution of our work is integrating all of the mathematical, algorithmic, and GPGPU-based high-performance computing code implementation components together into an accurate and computationally effective

simulator specifically targeting permeability estimation. In this paper, we also quantitatively demonstrate the robustness, accuracy, and computational efficiency of the resulting simulator on large-scale problems that were largely not computationally accessible before.

Recently, the MRT-LBM implementation discussed in this paper has been used for rapid evaluations of the effect of segmentation threshold on permeability computation [62], benchmarking pore-scale flow simulators for permeability estimation [61], and representative elementary volume (REV) estimation for digital rock permeability [63]. A total of 1500 permeabilities were computed for five rock samples of size 1024×1024×1024 in [62]. One hundred segmentation realizations were generated for each rock and permeabilities were computed in the x, y, and z directions.

We briefly describe the MRT-LBM algorithm and its code implementation. The accuracy of MRT-LBM is validated by use of microstructures of geometries for which analytical and semi-analytical expressions for absolute permeability exist. As part of the validation work, we also compare the computed permeability of digital rocks with that measured in the laboratory for two rock types. Distributed parallel performance of MRT-LBM is evaluated for a realistic sphere pack and a panoply of rock image volumes acquired for clastic and carbonate rocks, including Fontainebleau sandstone, Castlegate sandstone, and Grosmont carbonate. We report the computed permeabilities in all three (x, y, and z) directions for the microstructures used in the scalability tests. Whenever available, we provide measured permeability of these rocks from which the image sample is taken. Microstructures of drastically different resolutions for the above-listed rocks are purposefully utilized to fully probe and quantify the scalability characteristics of the MRT-LBM implementation. We also briefly describe an example use of the velocity fields generated by MRT-LBM for REV investigations. Finally, we provide a summary of the work and established conclusions.

2 Multiple-relaxation-time lattice Boltzmann method

We utilize a novel implementation of LBM to estimate the permeability of binary microstructures. The LBM solves a discrete, meso-scale form of the Boltzmann equation [30], which reduces to the incompressible Navier-Stokes equation in the low Mach number limit [41, 42]. Furthermore, the LBM solves the Stokes equation in the low Reynolds number regime permitting the definition of "permeability" as a concept. The LBM approach is commonly used to study flow in porous media at the pore scale [17, 24, 35, 47, 71] because of its computational efficiency and simplicity. It is very well suited to solve for the flow in complex geometries. For a general introduction to the lattice Boltzmann theory, we refer to [8, 34, 70, 71]. Most LBM implementations for pore-scale simulation utilize the BGK collision operator [13] for halfway bounce-back scheme at solid-fluid boundaries. However, the BGK approach suffers from deficiencies such as viscosity-dependent slip at the walls [31] and numerical instabilities when the Reynolds number is relatively high (i.e., the relaxation time is pushed to the limit of 0.5). Thus, it is difficult to obtain the "ground truth" flow properties of a porous medium with the BGK method.

On the other hand, the MRT technique provides an effective cure to these deficiencies and offers greater flexibility for capturing complex flow physics [21, 43]. Thus, the MRT technique is implemented to the computational engine of the LBM-based code for permeability estimation used in this work. In the MRT technique, the distribution function is transformed into a set of moments, each of which may be relaxed with an individual rate [21, 43]. When a single-relaxation-time approach is used, strong spurious velocities may originate from long-range contributions to the equilibrium distribution functions from the bounce-back boundary conditions. Introducing an MRT technique significantly suppresses spurious velocities [21, 55]. This is achieved by eliminating the effect of the non-hydrodynamic modes by setting the relaxation time for these modes to 1.0, which results in automatically setting the distribution functions to their equilibrium values at each time step. Moreover, it has been demonstrated that the introduction of the MRT approach improves the numerical stability of the algorithm for two-phase two-component flow [36]. Viscosity independence is also achieved for the bounce-back boundary conditions [53] by tuning the relaxation parameters that correspond to the non-hydrodynamic modes. Although boundary interpolation schemes demonstrate slightly more consistent behavior [16, 25], it has been found that the standard bounce-back method gives accurate results for flow in complex porous media [26, 66]. Thus, the standard bounce-back method is implemented in MRT-LBM for computational efficiency. In that sense, our implementation of the MRT technique is similar to the one described in [26]. However, our implementation differs from it in various significant aspects. Our MRT-LBM algorithm does not take advantage of the transformation of the distribution function originally proposed by [65] and later enhanced by [26] for improved accuracy using single precision arithmetic. We rather directly use double precision arithmetic in our implementation of the MRT-LBM code.

The fluid is driven by a body-force term in MRT-LBM by use of a loop boundary condition imposed on the inlet and outlet faces of the domain. The loop boundary condition is

similar to the popular periodic boundary condition but does not require mirroring of the domain. A fluid package that exits the domain at a given domain-boundary surface (e.g., outlet) enters into the domain at the opposing boundary-surface (e.g., inlet) under the effect of the same body force, so long as there is a fluid cell at the entry point. A precise treatment of body force is a requirement to eliminate the error terms in velocity gradients [28]. The body force implementation by [27, 40] is incorporated into the MRT-LBM. The MRT method is described in detail in [21, 55]. There are two options for the domain boundaries perpendicular to the main flow direction, namely, the loop boundary condition and the no-flow (i.e., closed) boundary condition. The zero-slip boundary condition (for the velocity vector) is imposed on the surfaces between rock-grains (solid) and fluid saturating the pore space. We briefly describe the main elements of the MRT method below by closely following the formalism of [26]:

The MRT computations operate with the following steps: First, the macroscopic node variables, namely density ρ and velocity $\mathbf{u}$ are obtained from the distribution function $\mathbf{f}(\mathbf{x}, t)$ through the following equations:

$$\rho = \sum_{i=0}^{18} f_i, \tag{1}$$

and

$$\rho \mathbf{u} = \sum_{i=0}^{18} \mathbf{e}_i f_i + \frac{\rho \mathbf{g}}{2}. \tag{2}$$

The definition for velocity is according to the forcing scheme of [27], where $\mathbf{g}$ is a body force and $\mathbf{e}_i$ is the ith component of the velocity vectors at each node. We use the D3Q19 lattice structure for the velocity vectors, hence $i = 0, \cdots, 18$. Figure 1 illustrates 19 velocity vectors in 3D space (D3Q19 scheme), which are defined as

$$\mathbf{e} = c \begin{bmatrix} 0 & 1 & -1 & 0 & 0 & 0 & 0 & 1 & -1 & 1 & -1 & 0 & 0 & 0 & 0 & 1 & -1 & 1 & -1 \\ 0 & 0 & 0 & 1 & -1 & 0 & 0 & 1 & 1 & -1 & -1 & 1 & -1 & 1 & -1 & 0 & 0 & 0 & 0 \\ 0 & 0 & 0 & 0 & 0 & 1 & -1 & 0 & 0 & 0 & 0 & 1 & 1 & -1 & -1 & 1 & 1 & -1 & -1 \end{bmatrix}^T, \tag{3}$$

where $c = dx/dt$ is the lattice speed. The lattice spacing dx and time-step dt are both unity.

The equilibrium distribution $f^{\mathrm{eq}}(\rho, \mathbf{u})$ and forcing term $\mathbf{F}$ are then computed from the density and velocity of the node where the components are, respectively, computed by

$$f_i^{\mathrm{eq}}(\rho, \mathbf{u}) = \rho w_i \left[1 + 3\mathbf{e}_i \cdot \mathbf{u} + \frac{9}{2} (\mathbf{e}_i \cdot \mathbf{u})^2 - \frac{3}{2} \mathbf{u}^2 \right] \tag{4}$$

and

$$F_i = 3 w_i \left[\mathbf{e}_i \cdot \mathbf{g} + \mathbf{u}\mathbf{g} : (3\mathbf{e}_i \mathbf{e}_i - \mathbf{I}) \right]. \tag{5}$$

In the above equations, w_i is the weight coefficient for the corresponding velocity vector, given by $w_0 = 1/3$, $w_{1-7} = 1/18$, $w_{8-18} = 1/36$, and $\mathbf{I}$ is the identity matrix.

The post-collision distribution function $\mathbf{f}'(\mathbf{x}, t)$ is computed using the MRT operator

$$\mathbf{f}'(\mathbf{x}, t) = \mathbf{f}(\mathbf{x}, t) + \mathbf{M}^{-1} \left[\mathbf{S}\mathbf{M} \left(\mathbf{f}^{eq} - \mathbf{f} \right) + \left(\mathbf{I} - \frac{1}{2}\mathbf{S} \right) \mathbf{M}\mathbf{F} \right] \tag{6}$$

where $\mathbf{M}$ is the orthogonal matrix which transforms the distribution function into moment space and $\mathbf{M}^{-1}$ as its inverse. $\mathbf{S}$ is the diagonal matrix of relaxation rates for each moment. Further details of the MRT model can be found in [21]. Finally, the post-collisional distribution is streamed to the neighboring nodes by

$$f_i(\mathbf{x} + \mathbf{e}_i dt, t + dt) = f_i'(\mathbf{x}, t) \tag{7}$$

Permeability for a given flow direction is computed using the following formula

$$k_i = \frac{Q_i \mu}{A \mathbf{g}}, \tag{8}$$

where the subscript index i runs as x, y, and z; Q_i denotes the flux in a given flow direction; μ is the fluid viscosity; A is the total surface area for single-phase flow. Since we define the flux in a given direction as follows in our implementation

$$Q_i = \tilde{u}_i \phi A, \tag{9}$$

where $\tilde{u}_i$ represents the average velocity in a given direction and ϕ denotes the porosity. Then, the permeability equation becomes

$$k_i = \frac{\tilde{u}_i \phi \mu}{\mathbf{g}}. \tag{10}$$

Since k_i is in lattice units, we multiply Eq. 9 with the squared value of voxel resolution (specified in $[1.0 \times 10^{-6}\mathrm{m} = \mu\mathrm{m}]$) to convert to [Darcy] and then with 1.0×10^3 to convert to [mDarcy].

3 Parallel GPGPU implementation

A recent development in scientific computing is conducting high-performance numerical computations on GPGPUs. GPGPUs were developed in the 1990s to accelerate the rendering of images (2D and 3D) for output to a display. Since then, the stream processing capabilities of GPGPUs have

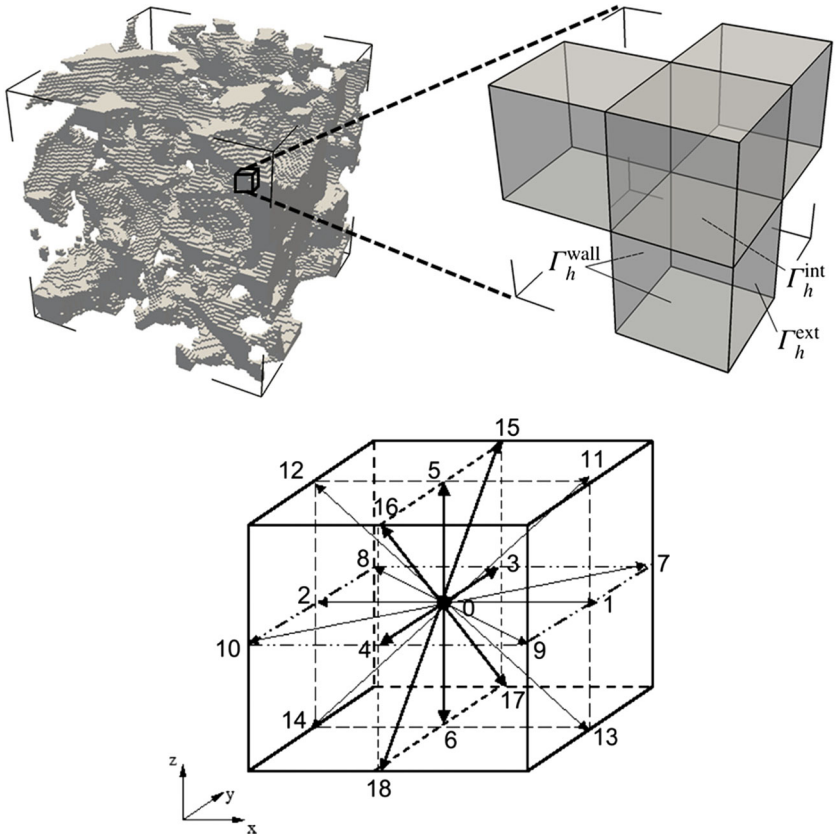

Fig. 1 An example computational domain and its conceptualization (top frame) for direct numerical simulation including various types of boundary definitions per lattice element (i.e., internal solid-fluid boundary (solid wall), $\Gamma_{\mathbf{h}}^{\mathbf{wall}}$; external domain surface, $\Gamma_{\mathbf{h}}^{\mathbf{ext}}$; internal solid-solid boundary, $\Gamma_{\mathbf{h}}^{\mathbf{int}}$). The lattice structure of the D3Q19 scheme with 19 velocity components (adapted from [56]) (bottom frame)

been focused on scientific computing, and the application to scientific computing has led to commercial lines of GPGPUs that have thousands of double-precision computation cores with error checking. GPGPU computation can become much faster (e.g., 10–1000 times faster compared to CPU computation) if a problem, or computation, lends itself well to many lightweight computation threads such as the collision and propagation kernels of LBM. In fact, a number of LBM implementations have already been made taking advantage of GPGPU computing, e.g., [11, 14, 72]. More recently, [19] demonstrated the use of CUDA and OpenCL in the optimization of a BGK-based LBM implementation on heterogeneous computing platforms. None of the above references demonstrate a 3D implementation of the MRT-LBM algorithm taking advantage of multi-node GPGPU computing.

A novel massively parallel hardware-dedicated implementation of the above-discussed MRT-LBM algorithm is made for NVIDIA GPGPU cards by use of the CUDA programming language. CUDA is a variant of the C++ programming language with extra functions to control the device (GPGPU) from the host (CPU). In addition, the MRT-LBM code utilizes a one-dimensional domain decomposition scheme with a single ghost-layer communicating the solutions along domain boundaries (Fig. 2). The domain decomposition communications are managed by use of message passing interface (MPI). For brevity, the MRT-LBM code is also referred to as MRT-LBM in the text.

Simulations with MRT-LBM are performed on a large Linux-based CPU-GPGPU HPC cluster. In order to minimize the impact on other users, unless otherwise stated, all simulations are performed using only four cluster nodes each with two Tesla K80 GPGPU cards. The technical specification of each CPU-GPGPU node is as follows: HP Proliant XL250a Gen9, 24 Cores - Intel(R) Haswell - Xeon(R) CPU E5-2680 v3 @ 2.50 GHz, 256-GB DRAM, 0.8 TB/scratch, 10 Gbps Ethernet, 56 Gbps fully non-blocking FDR (FBB) Infiniband), and 2 Tesla K80 GPGPU cards per node. It is important to note that each Tesla K80 has ∼5000 CUDA cores and 24 GB of RAM. Therefore, the compute resource dedicated to each run can be summarized with ∼40,000 CUDA cores and ∼200 GB of RAM. On average, the MRT-LBM code required ∼60 GB of RAM for a given simulation. The simulations utilized 100% of the GPGPU nodes' processing potential. In other words, no two simultaneous simulation jobs were submitted to the same GPGPU nodes.

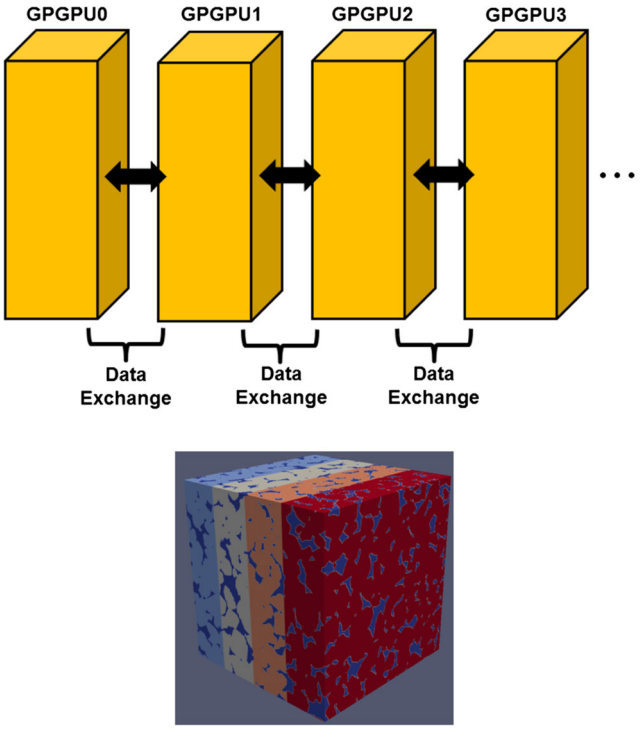

Fig. 2 Schematic description of the 1D domain decomposition approach with asynchronous data change is shown in the top frame. The model slices represented by varying colors in the bottom frame indicate the decomposition of the simulation domain by use of the 1D domain decomposition approach implemented in MRT-LBM. Four GPGPUs (one cluster node) are used with MRT-LBM

4 Validation

First set of validation tests are conducted using geometries for which analytical or semi-analytical solutions for permeability exist. First, we briefly review these solutions below:

Darcy's law states that the volume flux Q of a viscous fluid per unit time, through a sample of porous material is linearly proportional to the pressure difference ΔP applied to the opposite faces of the porous sample and the cross-section area A, and inversely proportional to the fluid viscosity μ and sample length L:

$$Q = -k\frac{A}{\mu}\frac{\Delta P}{L} \tag{11}$$

for creeping flow, i.e., at low Reynolds numbers [29]. The proportionality constant k is a fundamental property of the porous medium referred to as the absolute permeability, which has units of length squared. The most common permeability unit is Darcy or milliDarcy (mD), such that 1 Darcy $\cong 10^{-12}$ m^2 and 1 mD $\cong 10^{-15}$ m^2. In general, for a specific sedimentary rock, permeability increases with grain size and porosity but in a non-unique manner.

The exact expressions for incompressible viscous flow through circular, square, and equilateral triangular cross-sections are known [48]. The permeability of a circular cross-section with radius R is given by

$$k = \frac{\pi}{8}\frac{R^4}{A}. \tag{12}$$

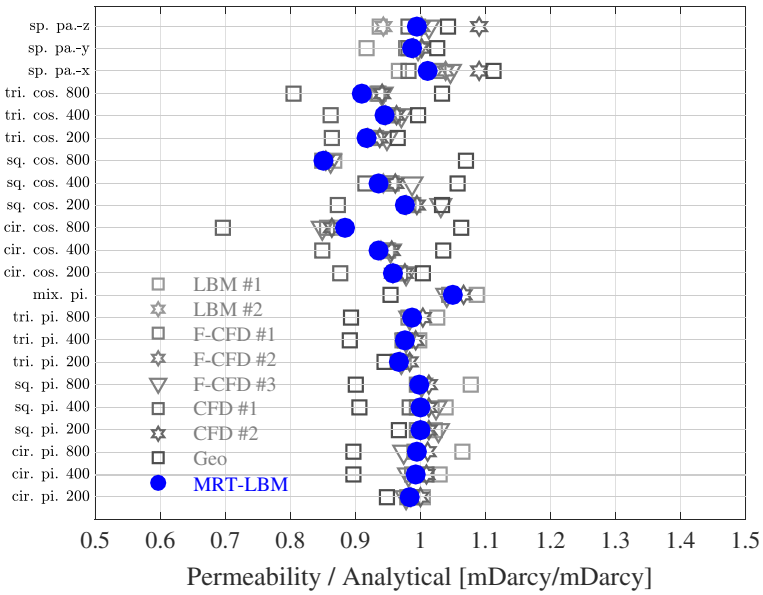

Fig. 3 Comparison of the MRT-LBM and analytical/semi-analytical solutions for permeability used in the validation test cases including results obtained for eight alternative methods. Numerically computed permeability values are normalized by the ones computed by analytical/semi-analytical solutions

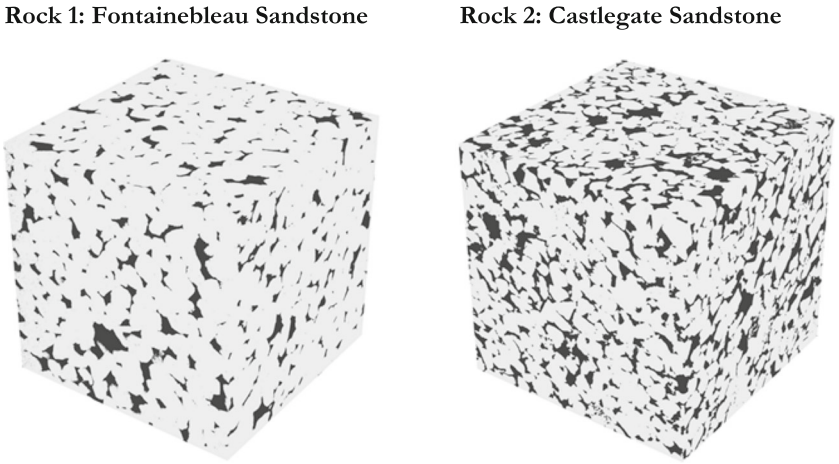

Fig. 4 Digital rock microstructures used in the validation tests [61]

Similarly, for a square cross-section pipe whose side is l

$$k = 0.035144\frac{l^4}{A}, \tag{13}$$

and for a pipe of triangular cross-section with a uniform side length l is given by

$$k = \frac{\sqrt{3}l^4}{320A}. \tag{14}$$

Various authors [67–69] report approximate expressions for flow in a pipe (of arbitrary cross-section) with sinusoidally varying radius. Sochi [69] derives pressure drop (p) across a sinusoidal pipe as

$$p = LQ\eta\frac{2(R_{\max}+R_{\min})^3+3(R_{\max}+R_{\min})(R_{\max}-R_{\min})^2}{2\pi(R_{\max}R_{\min})^{7/2}}. \tag{15}$$

In Eq. 14, $R_{\max}$ and $R_{\min}$ are the maximum and minimum radii, respectively. Using Eq. 14, we can calculate the change in permeability of a pipe as its diameter varies sinusoidally.

Analytical solutions for non-pipe 3D microstructures are also known in some cases. For instance, many approximate expressions for permeability of sphere packs have also been proposed [32, 33, 57, 74]. Rumpf and Gupte [57] suggest an expression for the permeability of monodisperse sphere packs

$$k = \frac{\phi^{5.5}D^2}{5.6}. \tag{16}$$

In Eq. 15, ϕ is the sphere pack porosity and D is the sphere diameter.

Validation tests are performed for several geometries with an analytical/semi-analytical solution for permeability. These geometries were documented in [61] and their brief descriptions are as follows:

(a) Three two-dimensional structures, which are each permeated with a single pipe of circular cross-section that is parallel to the flow direction (cir. pi. 200, cir. pi. 400, and cir. pi. 800).
(b) Three two-dimensional structures, which are each permeated with a single pipe of square cross-section that is parallel to the flow direction (sq. pi. 200, sq. pi. 400, and sq. pi. 800).

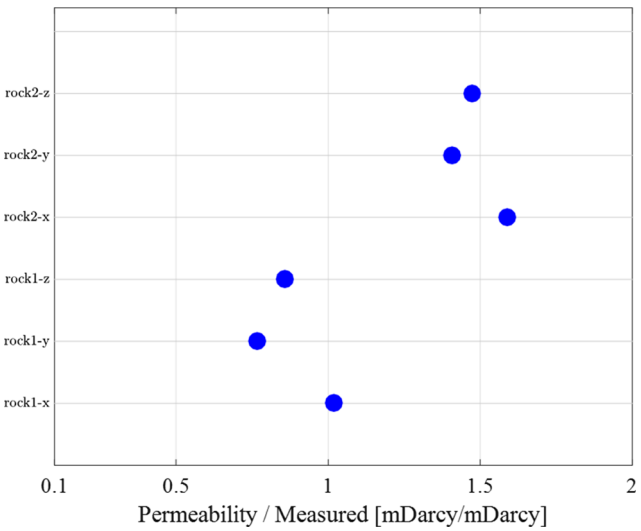

Fig. 5 Computed permeability normalized by laboratory measurements

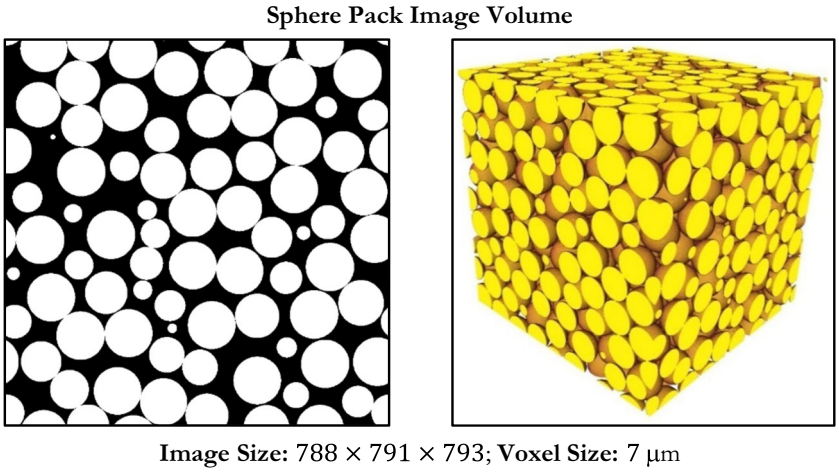

Fig. 6 2D and 3D example views of the sphere pack pore-scale image volume. The discrete image of the sphere pack geometry is reported in [2]

(c) Three two-dimensional structures, which are each permeated with a single pipe of equilateral triangle cross-section that is parallel to the flow direction (tri. pi. 200, tri. pi. 400, and tri. pi. 800).
(d) One two-dimensional structure which is permeated with four circular cross section pipes of various diameter that are parallel to the flow direction (mix. pi.).
(e) Twelve structures with sinusoidally varying cross-sections in the flow direction (cosine function) modified from (a)–(c) (cir. cos. 200, cir. cos. 400, cir. cos. 800, sq. cos. 200, sq. cos. 400, sq. cos. 800, tri. cos. 200, tri. cos. 400, and tri. cos. 800).
(f) One three-dimensional pack of identical spheres permeable in all three directions (x, y, and z), which will also be used in parallel scalability investigations [sp. pa.-x, sp. pa.-y, and sp. pa.-z].

Permeability values computed by use of MRT-LBM are compared with analytical/semi-analytical solutions (11–15) for the above-described geometries in Fig. 4. MRT-LBM solutions are compared not only against analytical solutions but also to the ones stemming from eight alternative simulation methods varying from alternative LBM implementations to conventional (and computationally intensive) Eulerian CFD techniques. Investigated techniques include an approximate geometric approach as well. Detailed description of these methods is kept beyond the scope of this paper. We refer the reader to [61] for a detailed benchmarking study involving MRT-LBM and alternative methods. The overall agreement of MRT-LBM solutions with analytical results is in general within ±10% except for two cases involving two large bore sinusoidal pipes. All numerical solution techniques including MRT-LBM exhibit a relatively larger departure from the analytical solution and a larger spread among predicted permeability values in the top part of Fig. 3, which contains relatively more complex geometries such as sinusoidal pipes and a sphere pack in which flows are simulated in three different (x, y, and z) directions. Analytical solutions for permeability are asymptotic approximations for these cases. Moreover, we must note that the known analytical solutions for pipes (of infinite length) cannot be considered as "exact" solutions for the investigated digital microstructures, since the digital microstructures are both finite in length and voxelated in surface texture. It is evident that uncertainties associated with the approximate nature of both (reference) semi-analytical and numerical solutions for sinusoidal pipes have a notable effect in the comparison as the calculated

Table 1 Permeability computation results for the sphere pack pore-scale image volume (porosity = 34.3%)

Reference permeability (mD)	Flow direction	Permeability (mD) MRT-LBM (GPGPU) Loop BC	Permeability (mD) MRT-LBM (GPGPU) No-flow BC
221,587–270,220	X	272,285	254,301
	Y	258,301	241,036
	Z	262,750	247,867

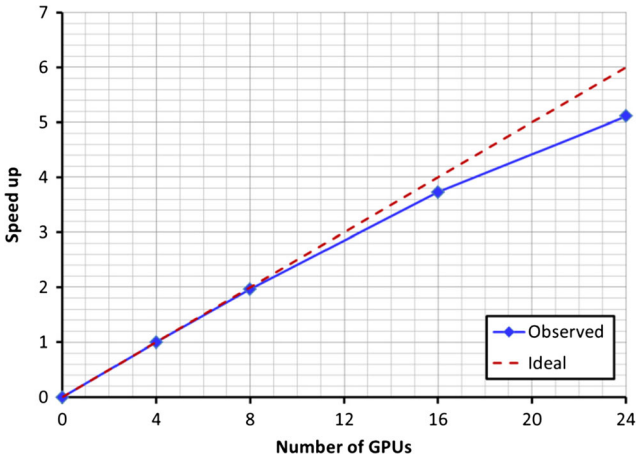

Fig. 7 Parallel scalability results for the sphere pack image volume. Loop boundary conditions are used at global domain boundaries

permeabilities using investigated solvers are more spread out with respect to reference solutions. Having stated that, for sinusoidal pipes, MRT-LBM predictions of permeability are reasonably accurate considering the large variability in the predicted permeabilities by all solvers. In the case of the sphere pack, which is the closest idealized geometry to a real rock, the numerical permeability values predicted by MRT-LBM are in very good agreement with the analytical solution (15). Overall, MRT-LBM delivers an accuracy level that is better than the aggregate trend obtained from eight alternative methods. In fact, MRT-LBM is one of the most accurate methods (Fig. 3).

As part of the validation work, we also compare the computed permeability of digital rocks with that measured in the laboratory for two rocks: Rock 1 is from the Fontainebleau formation which is a sub-rounded to rounded Oligocene age sandstone that has a mean grain size of approximately 450 μm and is moderately well sorted with a Trask coefficient of 1.43. Roughly 20% of the samples are quartz cement, leaving relatively low porosity of approximately 12%. Rock 2 is from the Castlegate formation of Utah which is a sub-angular to sub-rounded Mesozoic sandstone that has a mean grain size of approximately 350 μm and is moderately sorted with a Trask sorting coefficient of 1.69. Petrologic assessment of the sample indicates a minimal quartz cement volume of between 2 and 3% with similar amounts of carbonate cement and approximately 19% macro-porosity. Digital rock image volumes used in this study (each of size 1024×1024×1024) are shown in Fig. 4 for Rock 1 and Rock 2.

Direct comparison between digitally computed and laboratory measured permeability is indeed difficult due to many reasons: Firstly, laboratory measurements for this study were stressed whereas digital images were acquired under ambient pressure. Secondly, the two sets of results are obtained at different scales, DRP computations were carried on 2-mm-sized samples whereas laboratory measurements were performed on 25-mm cylindrical core plugs. Thirdly, the binarized digital images are subject to substantial uncertainty by the imaging and image processing workflow [44]. Finally, in this study, DRP computations do not sample identical portions of the rock used in the laboratory measurements. The computed porosities of the digital rock image volumes were found to be close to the laboratory measured porosity. Overall, we find that digitally computed permeability agrees reasonably well with laboratory measured permeability for the investigated rocks (Fig. 5).

5 Permeability computation and distributed parallel scalability

The computational performance of the MRT-LBM algorithm is evaluated from the accuracy and distributed parallel scalability perspectives for a sphere pack and three

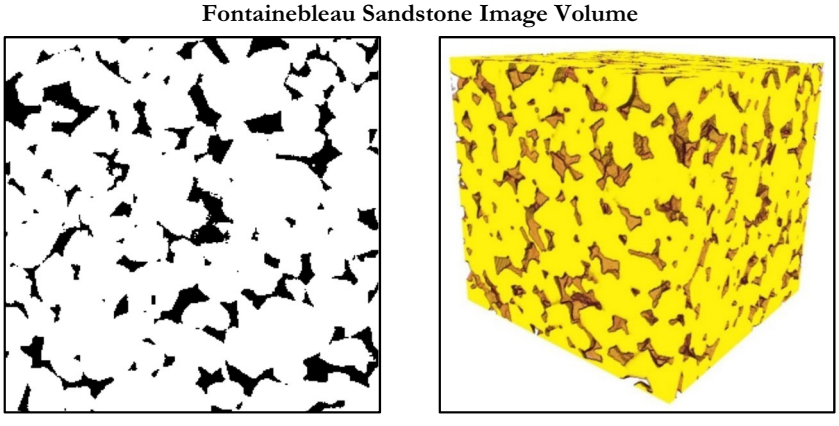

Fig. 8 2D and 3D example views of the Fontainebleau sandstone pore-scale image volume

Table 2 Permeability computation results for the Fontainebleau sandstone pore-scale image volume (porosity = 14.7%)

Measured permeability (mD)	Flow direction	Permeability (mD) Reference algorithm (CPU)	Permeability (mD) MRT-LBM (GPGPU) Loop BC	Permeability (mD) MRT-LBM (GPGPU) No-flow BC	Speed-up (Loop BC)
~1100	*X*	1626.92	1259.0	1126.2	17.0
	Y	1412.90	1180.9	1105.2	23.7
	Z	1698.94	1392.9	1327.0	21.8

benchmark rocks, namely, Fontainebleau sandstone, Grosmont carbonate, and Castlegate sandstone. One of the central underlying assumptions of the work is that the solid and pore space is accurately resolved in the microstructures representing the porous media. In other words, the effects of imaging, image processing [44, 62], and meshing uncertainties (e.g., [63, 66]) are kept beyond the scope of the paper. Moreover, for permeability computation problems used as realistic background for exploring the scalability characteristics of the code, detailed investigations involving image size and resolution for establishing REV is also kept beyond the scope of the study. We refer the reader to [63] for REV studies conducted by use of MRT-LBM.

5.1 Sphere pack

Packs of spherical grains are classical models of porous media. They serve as proxies for sedimentary granular geomaterials. A three-dimensional random pack of identical spheres was constructed by use of a granular dynamics discrete element simulation and utilized in a benchmarking study by [2, 3] (Fig. 6). The sphere pack is discretized with a uniform Cartesian grid. It was sampled using a voxel length of 7μm, corresponding to 100 voxels per grain diameter and resulting in a total image volume of 788×791×793 voxels. The sphere pack is permeable in all three (x, y, and z) directions. The porosity of the sphere pack is 34.3%.

Permeability computation results for the sphere pack image volume are documented in Table 1 together with the reference permeability range reported by [2]. For permeability computations, both loop and no-flow boundary condition cases are investigated for domain boundaries perpendicular to the main flow direction. The computed permeability range of 241,036–272,285 mD agrees well with the reference permeability range of 221,587–270,220 mD from [2].

Parallel scalability results for the sphere pack are illustrated in Fig. 7. Loop boundary conditions are used at global domain boundaries for the scalability tests. MRT-LBM implementation scales very well for the sphere pack problem with a parallel efficiency of ~85% on 24 GPGPUs. From the parallel scalability viewpoint, the optimal number of GPGPUs is 8–16 beyond which the parallel scalability starts to become affected by internode communications.

5.2 Fontainebleau sandstone

The Fontainebleau sandstone sample image was originally reported in [2]. This image has a voxel scale of 7.5 μm. Figure 8 shows the segmented binary digital rock (288×288×300) with grain and pore voxels. The model slices represented by varying colors in the top frame indicate the decomposition of the simulation domain by use of the 1D domain decomposition approach implemented in MRT-LBM. For this sample, the porosity is 14.7%, and permeability is between 1100 and 2000 mD [3, 34].

Permeability computation results for the Fontainebleau sandstone pore-scale image volume are documented in Table 2 together with the measured permeability of the core-plug from which the image sample is taken. For

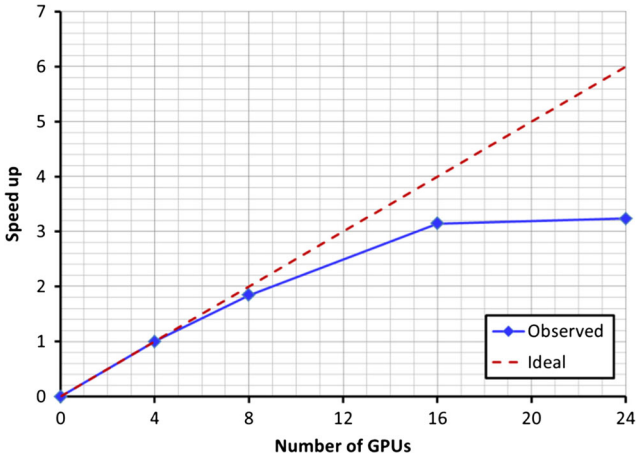

Fig. 9 Parallel scalability results for the Fontainebleau sandstone image volume. Loop boundary conditions are used at global domain boundaries

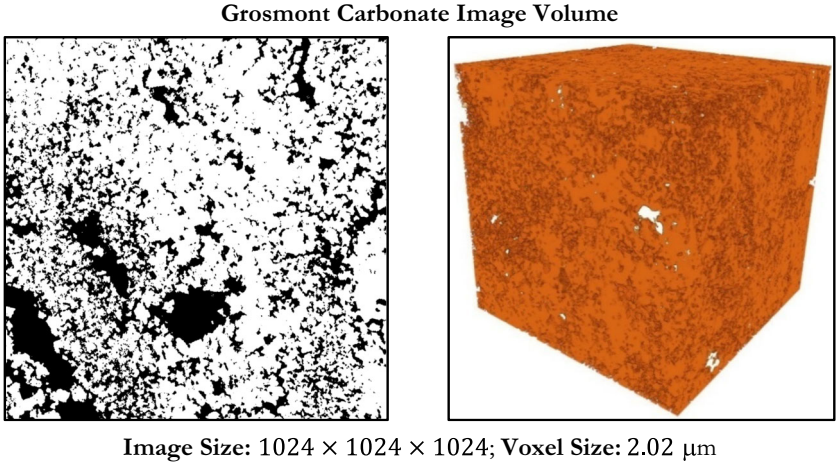

Fig. 10 2D and 3D example views of the Grosmont carbonate pore-scale image volume. The CT scan volume of the Grosmont carbonate sample is reported in [2]

permeability computations, both loop and no-flow boundary condition cases are investigated for global domain boundaries perpendicular to the main flow direction. The computed permeability range of 1105–1393 mD agrees well with the experimentally measured permeability of ∼1,100 mD.

Parallel scalability results for the Fontainebleau sandstone image volume are illustrated in Fig. 9. Loop boundary conditions are used at global domain boundaries for scalability tests. The optimal number of GPGPUs is eight beyond which the parallel scalability starts degrading. The communication costs significantly affect the parallel scalability beyond 16 GPGPUs.

5.3 Grosmont carbonate

The carbonate sample was taken from [2]. The sample was extracted from the Grosmont formation, Alberta, Canada. Figure 10 shows the digital rock sample of size 1024×1024×1024. The voxel edge length is 2.02 μm. The sample porosity is 24%, and laboratory-measured permeability ranges from 150 to 470 mD.

Permeability computation results for the Grosmont carbonate pore-scale image volume are documented in Table 3 together with the measured permeability of the core-plug from which the image sample is taken. For permeability computations, both loop and no-flow boundary condition cases are investigated for global domain boundaries perpendicular to the main flow direction. The computed permeability range of 412–938 mD differs from the measured permeability range of 150–470 mD. Excluding the computed permeability in the z direction gives rise to a computed permeability range of 412–534 mD, which is relatively more consistent with the high end of the measured permeability range. The difference between measured and computed permeability ranges indicate that the image sample may not be sufficiently large to be a representative elementary volume. It is important to note that, in general, carbonate rocks are significantly more heterogeneous compared to clastic rocks.

Table 3 Permeability computation results for the Grosmont carbonate pore-scale image volume (porosity = 27.2%)

Measured permeability (mD)	Flow direction	Permeability (mD) MRT-LBM (GPGPU) Loop BC	Permeability (mD) MRT-LBM (GPGPU) No-flow BC
150–470	X	443.5	412.2
	Y	533.6	486.4
	Z	937.8	884.4

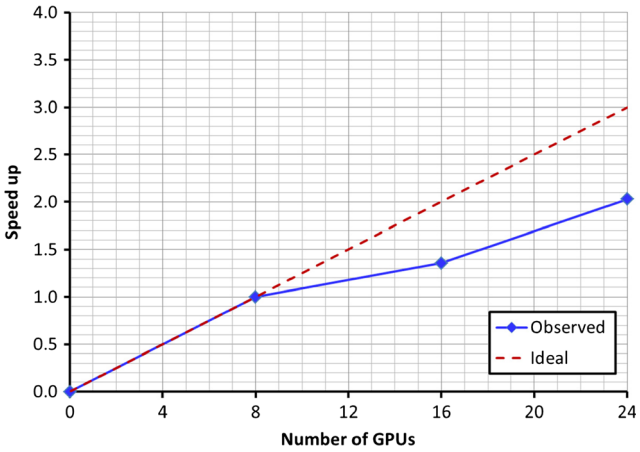

Fig. 11 Parallel scalability results for the Grosmont carbonate image volume. Loop boundary conditions are used at global domain boundaries

Parallel scalability results for the Grosmont carbonate image volume are illustrated in Fig. 11. Loop boundary conditions are used at global domain boundaries for scalability tests. Communication costs affect the parallel scalability of the MRT-LBM beyond eight GPGPUs. The relatively more emphasized heterogeneity of the carbonate sample and the simple 1D domain decomposition approach, which divides the domain based on a uniform division of the total number of lattices along the main flow direction (Fig. 2). govern the parallel scalability behavior of MRT-LBM, and give rise to a relatively less smooth speed-up curve compared to the previously investigated cases. Having stated that, the scalability is still at ~67% on 24 nodes, which is acceptable.

Table 4 Permeability computation results for the Castlegate sandstone pore-scale image volume (porosity = 21.4%)

Flow direction	Permeability (mD) MRT-LBM (GPGPU) Loop BC	Permeability (mD) MRT-LBM (GPGPU) No-flow BC
X	1437.1	1376.0
Y	1272.1	1214.5
Z	1333.2	1278.5

Fig. 12 2D and 3D example views of the micro-CT image of the Castlegate sandstone (top frame). The CT scan volume of the Castlegate sample (bottom frames)

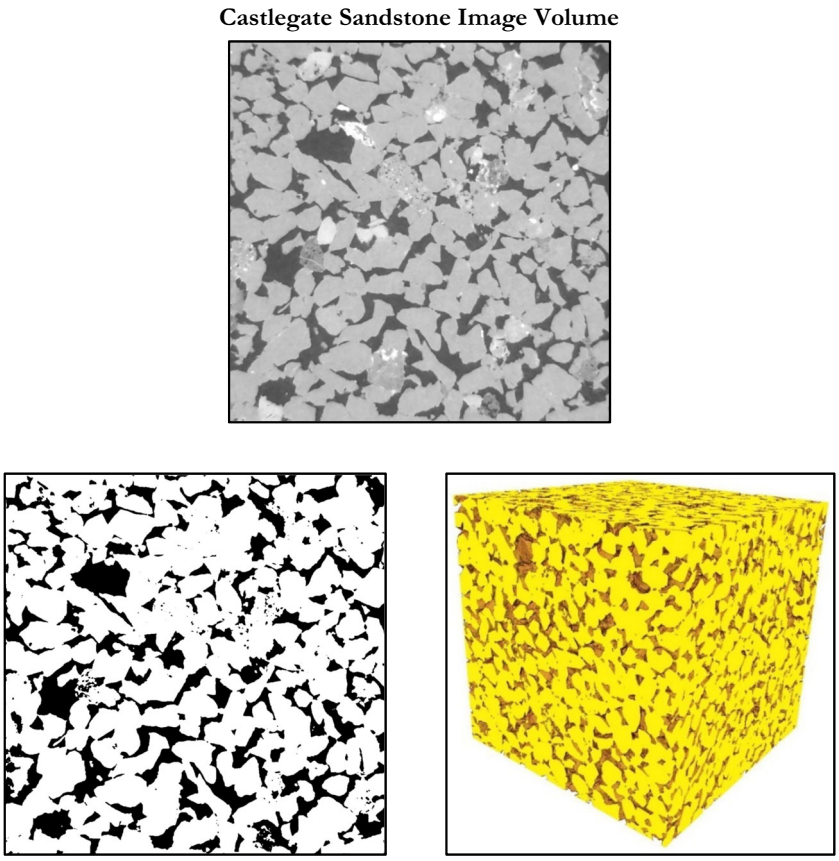

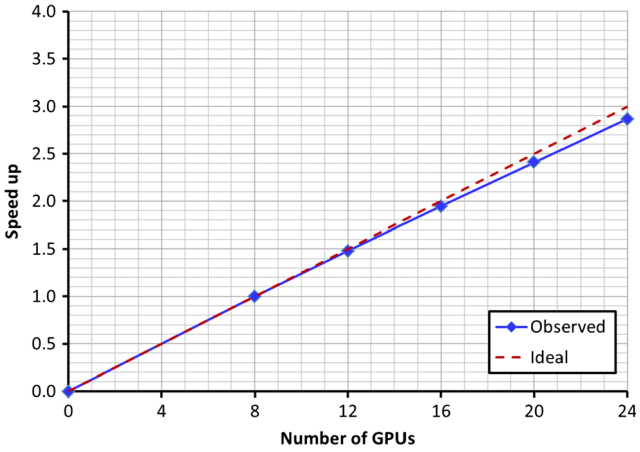

Fig. 13 Parallel scalability results for the Castlegate sandstone image volume. Loop boundary conditions are used at global domain boundaries

5.4 Castlegate sandstone

A detailed study is performed by use of various samples of the Castlegate rock with different porosities. We start with a 1024×1024×1024 image volume of voxel resolution 2.072 μm and porosity 21.4% (Fig. 12). We compute permeabilities for this image in x, y, and z directions using both loop and no-flow boundary conditions, separately. The results are documented in Table 4. Parallel scalability results for the Castlegate sandstone image volume are illustrated in Fig. 13. Loop boundary conditions are used at global domain boundaries for scalability tests. The scalability profile of the MRT-LBM implementation is near ideal with a parallel efficiency of ∼96% on 24 GPGPUs.

Subsequent to the above study, permeability computations are performed for 11 Castlegate sandstone images with porosities in the range of 17.9–26.8%. We compute permeabilities in all three (x, y, and z) directions using loop boundary conditions on global domain boundaries. Computed permeability results along with run time information are documented in Table 5. For all runs, four compute nodes are used each with two NVIDIA Tesla K80 GPGPU cards amounting to a total GPGPU count of 16. The computational performance results are also documented in terms of speed-up with respect to the run times delivered by a commercial reference tool on a comparable compute architecture (Table 5).

While individual results are not reported for brevity, the MRT-LBM and commercial tool computed permeability results are within 10 to 13% of each other depending on the flow direction. The differences in the computed permeability between MRT-LBM and the reference tool are in fact smaller than, for example, the computed permeability uncertainty that arises from the choice of segmentation threshold [62]. Nonetheless, at this point, it is important to emphasize the fact that it is unknown which tool's solutions are closer to "true" permeabilities. Having stated that, extensive validation tests performed for MRT-LBM, some of which were documented earlier in the paper, constitute quantitative evidence for the reliable accuracy level delivered by the MRT-LBM.

Larger versions the Castlegate sandstone image volume are generated through downscaling to explore the limits of

Table 5 Permeability computation results for the Castlegate sandstone pore image for various segmentation thresholds

Segmented image name	Porosity	Permeability (mD)			Run time (min)			Total run time (h)	Speed-up wrt. commercial tool		
	%	X	Y	Z	X	Y	Z		X	Y	Z
CG1_R-49	17.9	799	715	738	221	30.2	34.6	4.8	1	6	5
CG1_R-40	18.7	929	829	861	30.9	30.7	33.6	1.6	6	6	6
CG1_R-30	19.5	1070	952	993	30.8	29.3	36.2	1.6	9	8	5
CG1_R-20	20.2	1213	1077	1127	33.2	38.7	30.1	1.7	7	6	7
CG1_R-10	20.9	1361	1206	1265	29.1	27.7	30.4	1.5	8	9	7
CG1_R0	21.7	1520	1347	1414	157.5	27.8	29.8	3.6	1	11	7
CG1_R10	22.4	1682	1489	1562	28.3	27.1	29.2	1.4	8	8	8
CG1_R20	23.3	1884	1665	1746	28	26.7	29	1.4	8	9	10
CG1_R30	24.3	2126	1874	1965	27.3	29.8	28.2	1.4	9	8	10
CG1_R40	25.4	2426	2132	2235	27.3	36.9	30.5	1.6	9	8	8
CG1_R50	26.8	2818	2471	2591	27.5	25.3	27.8	1.3	10	16	11

Loop boundary conditions are used on global domain boundaries. Resources utilized for the runs: 4 compute nodes each with 2-Tesla K80 GPGPU cards. Each K80 card has ∼5000 CUDA cores and ∼24 GB of RAM (∼40,000 CUDA cores and ∼200 GB of RAM utilized)

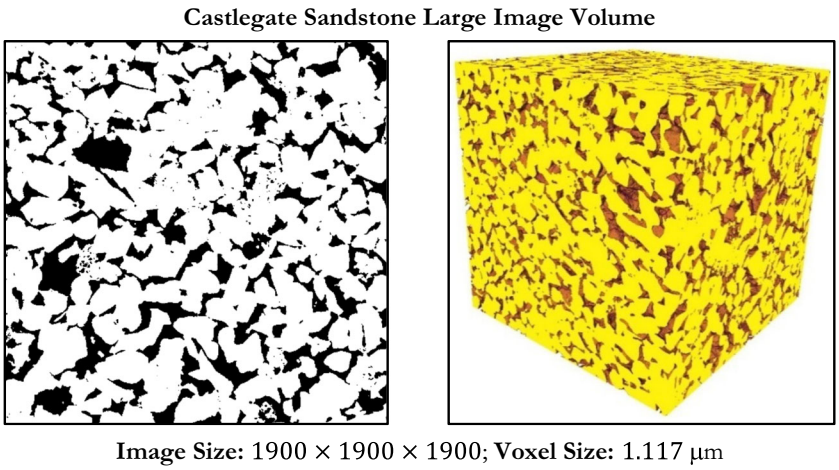

Fig. 14 2D and 3D example views of a large micro-CT image of a Castlegate sandstone

the permeability computation capability. An example large case of size 1900×1900×1900 (Fig. 14) is simulated on eight compute nodes by use of 32 GPGPUs for computing permeabilities in three dimensions using loop and no-flow boundary conditions. The permeability computation results are reported in Table 6 along with run time information, which varies between 261 to 324 min.

6 Representative elementary volume determination

The velocity fields generated by the MRT-LBM can be used to quantitatively and qualitatively investigate the effects of the image volume size and the boundary conditions (imposed on the global domain) on flow fields, and hence, on the computed digital rock permeability. The goal here is to identify the minimum image volume size and the boundary conditions that will lead to an analysis volume at which the flow fields internal to the domain are insensitive to these parameters, i.e., one of the definitions of REV for permeability, which differs from the commonly used averaging method definition [7]. An example study for a Berea sandstone microstructure is shown in Fig. 15 [63]. Single-phase flow simulations were performed with MRT-LBM on 1024×1024×1024, 768×768×768, 512×512×512, and 256×256×256 size image volumes. The central sub-cubes of size 256×256×256 were extracted from each of these simulations and the velocity fields are visualized on these sub-cubes. The simulations were performed for loop and no-flow boundary conditions on global domain boundaries that are perpendicular to the main flow direction. As the flow domain size increases, the velocity field in the central sub-cube becomes less sensitive to the domain size. Effects of global domain boundary conditions on the velocity field diminish with increasing domain size. Further details of the REV work for digital rock permeability can be found in [63].

In the above-mentioned study, the authors fix the computing domain center when performing REV tests. In order to account for the effect of spatial heterogeneity in a statistical fashion, one could also consider conducting statistical REV tests [76]. In this approach, one moves the computational domain throughout the entire sample space and evaluates the mean and standard deviation of the quantity of interest (e.g., permeability). Then, the computational domain size is increased and the process is repeated. It is expected that the standard deviation decreases

Table 6 Permeability computation results for the Castlegate sandstone large pore image

Segmented image name	Boundary condition	Porosity	Permeability (mD)			Run time (min)		
		%	*X*	*Y*	*Z*	*X*	*Y*	*Z*
CG1_2015_1900	Solid	21.4	1326.0	1169.7	1230.0	293.8	306.5	323.8
	Loop		1386.0	1226.2	1283.4	261.3	287.2	305.5

Resources utilized for the runs: 8 compute nodes each with 2-Tesla K80 GPGPU cards. Each K80 card has ∼5000 CUDA cores and ∼24 GB of RAM (∼80,000 CUDA cores and 384 GB of RAM utilized)

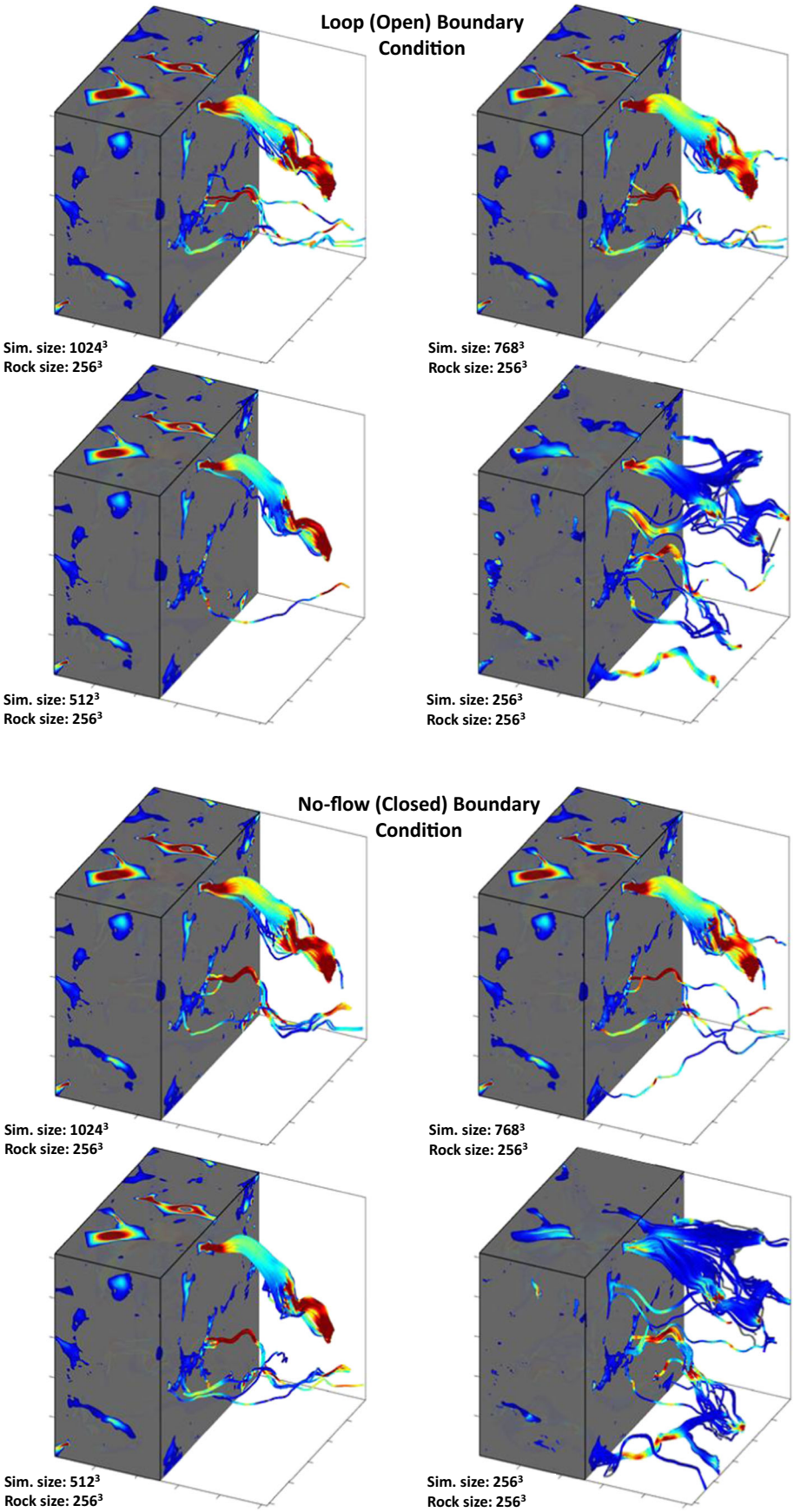

Fig. 15 Velocity fields computed by use of MRT-LBM within the framework of a REV study. Single-phase flow simulations were performed with MRT-LBM on 1024×1024×1024, 768×768×768, 512×512×512, and 256×256×256 size image volumes. The central sub-cubes of size 256×256×256 were extracted from each of these simulations and the velocity fields are visualized on these sub-cubes. The simulations were performed for loop and no-flow boundary conditions on global domain boundaries that are perpendicular to the main flow direction. Figure adapted from [64]

with the increase of the computational domain size. When the standard deviation is sufficiently small (compared to a specified criterion) and the computational domain size is sufficiently large, convergence to REV is declared. Although the authors did not perform statistical REV tests in the study reported in [63], the MRT-LBM code can readily be used in such a study.

7 Summary and conclusions

We describe and extensively test the distributed parallel implementation of an innovative LBM algorithm for simulating flow in pore-scale media based on the MRT model that utilizes a precise treatment of body force. As novel contributions to the scientific literature, we (1) integrate all of the mathematical, algorithmic, and high-performance computing (using GPGPUs) elements together with an optimized implementation in CUDA, and (2) provide quantitative results with the resulting simulator (MRT-LBM) in terms of robustness, accuracy, and computational efficiency for a variety of flow geometries including various types of real rock images. We report on extensive validations of the simulator in terms of accuracy and provide near-ideal distributed parallel scalability results on large pore-scale image volumes that were largely computationally inaccessible prior to our implementation.

The MRT-LBM code implementation is applied to the computation of absolute permeability in several validation cases and real-life 3D pore-scale images used in distributed parallel scalability tests. The following conclusions are reached as the results of validation, parallel scalability, and application studies:

- The MRT-LBM method delivers a good level of accuracy for computed permeability on microstructures for which an analytical or semi-analytical solution exist.
- The computed permeabilities agree well with reference measured permeabilities for investigated rocks.
- The distributed parallel GPGPU code implementation of the MRT-LBM algorithm scales well for large problems with larger than 1 billion voxels. It enables the simulation of pore-scale models with billions of voxels in the order of a few minutes to a few hours, thereby enabling fast and accurate permeability computations on real rock images.
- The velocity fields generated by MRT-LBM can be quantitatively and qualitatively utilized within REV investigations for digital rock permeability.
- The MRT-LBM simulator can serve as one of the key-enabler components of an integrated DRP workflow for permeability estimation.
- Future work will focus on utilizing MRT-LBM as a fast and efficient momentum balance solver for a two-phase two-component Helmholtz free-energy LBM-based pore-scale flow simulator.

Acknowledgments We thank Shell International Exploration and Production Inc. for permission to publish this paper. Farrel Gray's doctoral studentship was provided by the Qatar Carbonates and Carbon Storage Research Centre jointly funded by Qatar Petroleum, Shell and the Qatar Science and Technology Park.

References

1. Adler, P.M., Jacquin, C.G., Quiblier, J.A.: Flow in simulated porous media. Intern. J. Multiphase Flow **16**, 691–712 (1990)
2. Andrä, H., Combaret, N., Dvorkin, J., Glatt, E., Han, J., Kabel, M., Keehm, Y., Krzikalla, F., Lee, M., Madonna, C., Marsh, M., Mukerji, T., Saenger, E.H., Sain, R., Saxena, N., Ricker, S., Wiegmann, A., Zhan, X.: Digital rock physics benchmarks—part I: imaging and segmentation. Comput. Geosci. **50**, 25–32 (2013)
3. Andrä, H., Combaret, N., Dvorkin, J., Glatt, E., Han, J., Kabel, M., Keehm, Y., Krzikalla, F., Lee, M., Madonna, C., Marsh, M., Mukerji, T., Saenger, E.H., Sain, R., Saxena, N., Ricker, S., Wiegmann, A., Zhan, X.: Digital rock physics benchmarks—part II: computing effective properties. Comput. Geosci. **50**, 33–43 (2013)
4. ANSYS Inc: ANSYS FLUENT Theory Guide (2010)
5. Arns, C.H., Bauget, F., Limaye, A., Sakellariou, A., Senden, T., Sheppard, A., Sok, R.M., Pinczewski, V., Bakke, S., Berge, L.I., Oren, P., Knackstedt, M.: Pore-scale characterization of carbonates using x-ray microtomography. SPE J. **10**, 26–29 (2005)
6. Arns, C.H., Knackstedt, M.A., Pinczewski, W.V., Garboczi, E.J.: Computation of linear elastic properties from microtomographic images: methodology and agreement between theory and experiment. Geophysics **67**, 1396–1405 (2002)
7. Bear, J.: Dynamics of fluids in porous media. American Elsevier Publishing Company Inc., New York (1972)
8. Benzi, R., Succi, S., Vergassola, M.: The lattice Boltzmann-equation—theory and applications. Phys. Rep. **222**, 145–197 (1992)
9. Berg, S., Ott, H., Klapp, S.A., Schwing, A., Neiteler, R., Brussee, N., Makurat, A., Leu, L., Enzmann, F., Schwarz, J.-O., Kersten, M., Irvine, S., Stampanoni, M.: Real-time 3D imaging of Haines jumps in porous media flow. Proc. Nat. Acad. Sci. (PNAS) **110**, 3755–3759 (2013)
10. Berg, S., Rücker, M., Ott, H., Georgiadis, A., van der Linde, H., Enzmann, F., Kersten, M., Armstrong, R.T., de With, S., Becker, J., Wiegmann, A.: Connected pathway relative permeability from pore-scale imaging of imbibition. Adv. Water Res. **90**, 24–35 (2016)
11. Bernaschi, M., Fatica, M., Melchionna, S., Succi, S., Kaxiras, E.: A flexible high-performance lattice Boltzmann GPU code for the simulations of fluid flows in complex geometries. Concurr. Comput.: Prac. Exp. **22**, 1–14 (2010)
12. Berryman, J.G., Blair, S.C.: Use of digital image analysis to estimate fluid permeability of porous materials: application of two-point correlation functions. J. Appl. Phys. **60**, 1930–1938 (1986)
13. Bhatnagar, P.L., Gross, E.P., Krook, M.: A model for collision processes in gases. I. Small amplitude processes in charged and neutral one-component systems. Phys. Rev. **94**, 511–525 (1954)

14. Bisson, M., Bernaschi, M., Melchionna, S., Succi, S., Kaxiras, E.: Multiscale hemodynamics using GPU clusters. Commun. Comput. Phys. **11**, 48–64 (2012)
15. Blunt, M.J., Bijeljic, B., Dong, H., Gharbi, O., Iglauer, S., Mostaghimi, P., Paluszny, A., Pentland, C.: Pore-scale imaging and modelling. Adv. Water Res. **51**, 197–216 (2013)
16. Bouzidi, M.H., Firdaouss, M., Lallemand, P.: Momentum transfer of a Boltzmann-lattice fluid with boundaries. Phys. Fluids **13**, 3452–3459 (2001)
17. Cancelliere, A., Chang, C., Foti, E., Rothman, D.H., Succi, S.: The permeability of a random medium: comparison of simulation with theory. Phys. Fluids A **2**, 2085–2088 (1990)
18. Chen, H., Teixeira, C., Molvig, K.: Digital physics approach to computational fluid dynamics: some basic theoretical features. Intern. J. Modern Phys. C **8**, 675–684 (1997)
19. Chen, C., Wang, Z., Majeti, D., Vrvilo, N., Warburton, T., Sarkar, V., Li, G.: Optimization of lattice Boltzmann simulation with graphics-processing-unit parallel computing and the application in reservoir characterization. SPE J. **21**(3), 1425–1435 (2016)
20. COMSOL Multiphysics Documentation: COMSOL Multiphysics, version 5.3, Pore-scale flow. https://www.comsol.com/model/download/407771/models.ssf.porescaleflow.pdf. Accessed: 4 June 2017 (2017)
21. d'Humières, D., Ginzburg, I., Krafczyk, M., Lallemand, P., Luo, L.: Multiple-relaxation-time lattice Boltzmann models in three dimensions. Philos. Trans. Royal Soc. A **360**, 437–451 (2002)
22. Dvorkin, J., Armbruster, M., Baldwin, C., Fang, Q., Derzhi, N., Gomez, C., Nur, B., Nur, A., Mu, Y.: The future of rock physics: computational methods vs. lab testing. First Break **26**, 63–68 (2008)
23. Dvorkin, J., Derzhi, N., Diaz, E., Fang, Q.: Relevance of computational rock physics. Geophysics **76**, E141–E153 (2011)
24. Ferrèol, B., Rothman, D.H.: Lattice-Boltzmann simulations of flow through Fontainebleau sandstone. Transp. Porous Media **20**, 3–20 (1995)
25. Ginzburg, I., d'Humières, D.: Multireflection boundary conditions for lattice Boltzmann models. Phys. Rev. E **68**, 066614 (2003)
26. Gray, F., Boek, E.: Enhancing computational precision for lattice Boltzmann schemes in porous media flows. Computation **4**, 11 (2016)
27. Guo, Z., Zheng, C.: Analysis of lattice Boltzmann equation for microscale gas flows: relaxation times, boundary conditions and the Knudsen layer. Intern. J. Comput. Fluid Dyn. **22**, 465–473 (2008)
28. Guo, Z., Zheng, C., Shi, B.: Discrete lattice effects on the forcing term in the lattice Boltzmann method. Phys. Rev. E **65**, 046308 (2002)
29. Hassanizadeh, S.M., Gray, W.: High velocity flow in porous media. Transp. Porous Media **2**, 521–531 (1987)
30. He, X., Luo, L.S.: Theory of the lattice Boltzmann method: from the Boltzmann equation to the lattice Boltzmann equation. Phys. Rev. E **56**, 6811–6817 (1997)
31. He, X., Zou, Q., Luo, L., Dembo, M.: Analytic solutions of simple flows and analysis of nonslip boundary conditions for the lattice Boltzmann BGK model. J. Stat. Phys. **87**, 115–136 (1997)
32. Hinch, E.J.: An averaged-equation approach to particle interactions in a fluid suspension. J. Fluid Mech. **83**, 695–720 (1977)
33. Howells, I.D.: Drag due to the motion of a Newtonian fluid through a sparse random array of small fixed rigid objects. J. Fluid Mech. **64**, 449–476 (1974)
34. Keehm, Y.: Computational rock physics: Transport properties in porous media and applications. Ph.D. Dissertation, Stanford University, Stanford (2003)
35. Keehm, Y., Mukerji, T., Nur, A.: Permeability prediction from thin sections: 3D reconstruction and Lattice-Boltzmann flow simulation. Geophys. Res. Lett. **31**, L04606 (2004)
36. Kendon, V.M., Cates, M.E., Desplat, J.-C., Pagonabarraga, I., Bladon, P.: Inertial effects in three-dimensional spinodal decomposition of a symmetric binary fluid mixture: a lattice Boltzmann study. J. Fluid Mech. **440**, 147–203 (2000)
37. Knackstedt, M.A., Sheppard, A.P., Sahimi, M.: Pore network modelling of two-phase flow in porous rock: the effect of correlated heterogeneity. Adv. Water Res. **24**, 257–277 (2001)
38. Knackstedt, M.A., Arns, C., Madadi, M., Sheppard, A.P., Latham, S., Sok, R., Bächle, G., Eberli, G.: Elastic and flow properties of carbonate core derived from 3D X ray-CT images. SEG Tech. Prog. Expanded Abstr. **27**, 1804–1809 (2008)
39. Knackstedt, M.A., Latham, S., Madadi, M., Sheppard, A., Varslot, T., Arns, C.: Digital rock physics: 3D imaging of core material and correlations to acoustic and flow properties. Lead. Edge **28**, 28–33 (2009)
40. Kuzmin, A., Guo, Z., Mohamad, A.: Simultaneous incorporation of mass and force terms in the multi-relaxation-time framework for lattice Boltzmann schemes. Philos. Transac. Royal Soc. A Math. Phys. Eng. Sci. **369**, 2219–2227 (2011)
41. Ladd, A.J.C.: Numerical simulations of particulate suspensions via a discretized Boltzmann equation: part 1: theoretical foundation. J. Fluid Mech. **271**, 285–309 (1994)
42. Ladd, A.J.C.: Numerical simulations of particulate suspensions via a discretized Boltzmann equation: part 2. Numerical results. J. Fluid Mech. **271**, 311–339 (1994)
43. Lallemand, P., Luo, L.S.: Theory of the lattice Boltzmann method: dispersion, dissipation, isotropy, Galilean invariance, and stability. Phys. Rev. E **61**, 6546–6562 (2000)
44. Leu, L., Berg, S., Enzmann, F., Armstrong, R.T., Kersten, M.: Fast x-ray micro-tomography of multiphase flow in Berea Sandstone: a sensitivity study on image processing. Transp. Porous Media **105**, 451–469 (2014)
45. Llwellin, E.W.: LBflow: An extensible lattice Boltzmann framework for the simulation of geophysical flows. Part I: theory and implementation. Comput. Geosci. **36**, 115–122 (2010)
46. Llwellin, E.W.: LBflow: An extensible lattice Boltzmann framework for the simulation of geophysical flows. Part II: usage and validation. Comput. Geosci. **36**, 123–132 (2010)
47. Martys, N.S., Chen, H.: Simulation of multicomponent fluids in complex three dimensional geometries by the lattice Boltzmann method. Phys. Rev. E **53**, 743–750 (1996)
48. Mavko, G., Mukerji, T., Dvorkin, J. The rock physics handbook: Tools for seismic analysis of porous media, 2nd edn. Cambridge University Press, Cambridge (2009)
49. Meakin, P., Tartakovsky, A.M.: Modeling and simulation of pore-scale multiphase fluid flow and reactive transport in fractured and porous media. Rev. Geophys. **RG3002**, 1–47 (2009)
50. Otomo, H., Fan, H., Li, Y., Dressler, M., Staroselsky, I., Zhang, R., Chen, H.: Studies of accurate multi-component lattice Boltzmann models on benchmark cases required for engineering applications. J. Comput. Sci. **17**, 334–339 (2016)
51. Øren, P., Bakke, S., Rueslåtten, H.: Digital core laboratory: rock and flow properties derived from computer generated rocks. In: International Symposium of the Society of Core Analysts held in Trondheim, pp. 1–12, Norway (2006)
52. Palabos Documentation. http://www.palabos.org/documentation/userguide/. Accessed: 4 June 2017 (2017)
53. Pan, C., Luo, L.-S., Miller, C.T.: An evaluation of lattice Boltzmann schemes for porous medium flow simulation. Comput. Fluids **35**, 898–909 (2006)

54. Piller, M., Casagrande, D., Schena, G., Santini, M.: Pore-scale simulation of laminar flow through porous media. J. Phys.: Conf. Ser. **501**, 012010 (2014)
55. Premnath, K.N., Abraham, J.: Three-dimensional multi-relaxation-time (MRT) lattice-Boltzmann models for multiphase flow. J. Comput. Phys. **224**, 539–559 (2007)
56. Premnath, K.N., Pattison, M.J., Banerjee, S.: An investigation of the Lattice Boltzmann method for large eddy simulation of complex turbulent separated flow. J. Fluids Eng. **135**, 051401-1-12 (2013)
57. Rumpf, H.C.H., Gupte, A.R.: Einflüsse der Porosität und Korngröarticleßenverteilung im Widerstandsgesetz der Porenströmung. Chem. Ing. Tech. **43**, 367–375 (1971)
58. Saenger, E.H., Enzmann, F., Keehm, Y., Steeb, H.: Digital rock physics: effect of fluid viscosity on effective elastic properties. J. Appl. Geophys. **74**, 236–241 (2011)
59. Sain, R., Mukerji, T., Mavko, G.: How computational rock-physics tools can be used to simulate geologic processes, understand pore-scale heterogeneity, and refine theoretical models. Lead. Edge **33**, 324–334 (2014)
60. Saxena, N., Mavko, G.: Estimating elastic moduli of rocks from thin sections: digital rock study of 3D properties from 2D images. Comput. Geosci. **88**, 9–21 (2016)
61. Saxena, N., Hofmann, R., Alpak, F.O., Berg, S., Dietderich, J., Agarwal, U., Tandon, K., Hunter, S., Freeman, J., Wilson, O.B.: References and benchmarks for pore-scale flow simulated using micro-CT images of porous media and digital rocks. Adv. Water Res. **109**, 211–235 (2017)
62. Saxena, N., Hofmann, R., Alpak, F.O., Dietderich, J., Hunter, S., Day-Stirrat, R.: Effect of image segmentation andamp; voxel size on micro-CT computed effective transport andamp; elastic properties. Mar. Petrol. Geol. **86**, 972–990 (2017)
63. Saxena, N., Hofmann, R., Hows, A., Alpak, F.O., Freeman, J., Hunter, S., Appel, M.: Imaging and computational considerations for digital rock physics. Advances in Water Resources in review (2018)
64. Saxena, N., Mavko, G., Hofmann, R., Srisutthiyakorn, N.: Estimating permeability from thin sections without reconstruction: graphical study of 3D properties from 2D images. Comput. Geosci. **102**, 79–99 (2017)
65. Skordos, P.A.: Initial and boundary conditions for the lattice Boltzmann method. Phys. Rev. **48**, 4823–4842 (1993)
66. Shah, S.M., Gray, F., Crawshaw, J.P., Boek, E.S.: Micro-computed tomography pore-scale study of flow in porous media: effect of voxel resolution. Adv. Water Res. **95**, 276–287 (2016)
67. Sisavath, S., Jing, X., Pain, C.C., Zimmerman, R.W.: Creeping flow through an axisymmetric sudden contraction or expansion. J. Fluids Eng. **124**, 273–278 (2002)
68. Sisavath, S., Jing, X., Zimmerman, R.W.: Creeping flow through a pipe of varying radius. Phys. Fluids **13**, 2762–2772 (2001)
69. Sochi, T.: Newtonian flow in converging-diverging capillaries. Intern. J. Model. Simul. Scientific Comput. **4**, 1350011 (2013)
70. Succi, S.: The lattice boltzmann equation for fluid dynamics and beyond. numerical mathematics and scientific computation series. Clarendon Press, Oxford (2001)
71. Sukop, M.C., Thorne, D.T.: Lattice Boltzmann Modeling: An Introduction for Geoscientists and Engineers. Springer-Verlag, Berlin (2006)
72. Tölke, J.: Implementation of a lattice Boltzmann kernel using the compute unified device architecture developed by nVIDIA. Comput. Visual. Sci. **13**(1), 29–39 (2010)
73. Tölke, J., Baldwin, C., Mu, Y., Derzhi, N., Fang, Q., Grader, A., Dvorkin, J.: Computer simulations of fluid flow in sediment: from images to permeability. Lead. Edge **29**, 68–74 (2010)
74. Torquato, S.: Random Heterogeneous Materials: Microstructure and Macroscopic Properties. Springer Science & Business Media, New York (2002)
75. Wiegmann, A.: Computation of the permeability of porous materials from their microstructure by FFF-Stokes. Berichte des Fraunhofer ITWM, Nr. 129. Kaiserslautern, Germany (2007)
76. Zhang, D., Zhang, R., Chen, S., Soll, W.E.: Pore scale study of flow in porous media: scale dependency, REV, and statistical REV. Geophys. Res. Lett. **27**, 1195–1198 (2000)